Composition and strain contrast of Si1-xGex (x = 0.20) and Si1-yCy (y < 0.015) epitaxial strained films on (100) Si in annular dark field images

Wu, Xiaohua; Baribeau, Jean-Marc

Publisher's version / Version de l'éditeur:
https://doi.org/10.1063/1.3082019
Journal of Applied Physics, 105, 4, 2009

Composition and strain contrast of $Si_{1-x}Ge_x$ ($x=0.20$) and $Si_{1-y}C_y$ ($y \leq 0.015$) epitaxial strained films on (100) Si in annular dark field images

X. Wu[a] and J.-M. Baribeau
Institute for Microstructural Sciences, National Research Council Canada, Ottawa, Ontario K1A 0R6, Canada

(Received 5 November 2008; accepted 15 January 2009; published online 26 February 2009)

The annular dark field (ADF) image contrast of $Si_{1-x}Ge_x$ ($x=0.20$) and $Si_{1-y}C_y$ ($y \leq 0.015$) strained epitaxial films on (100) Si is investigated in a 200 kV scanning transmission electron microscope (STEM) with ADF detector inner semiangles ranging from 26 to 92 mrad. For the $Si_{1-x}Ge_x/Si$ system, the contrast increases with increasing ADF detector semiangle and decreases with increasing thickness to remain almost constant after the TEM sample thickness reaches 120 nm. The opposite trend is seen in the $Si_{1-y}C_y/Si$ system, where the contrast increases with increasing sample thickness and decreases with increasing ADF detector semiangle, and remains almost constant after the sample thickness exceeds 200 nm. In the dilute $Si_{1-y}C_y/Si$ system the lower average atomic number strained $Si_{1-y}C_y$ layers are brighter than the higher average atomic number Si for an ADF detector semiangle of up to 92 mrad when the sample thickness is greater than 200 nm. This anomalous contrast dependence is also observed for an ADF detector semiangle of up to 50 mrad in thinner TEM samples. The observed ADF-STEM image contrast is explained in relation to the atomic scattering and multislice simulations. The normalized intensity line scan profiles of ADF-STEM images coincide with the composition profiles determined from analytical TEM techniques: energy dispersive x-ray spectroscopy and electron energy loss spectroscopy, as well as secondary ion mass spectrometry. © *2009 American Institute of Physics*. [DOI: 10.1063/1.3082019]

I. INTRODUCTION

Semiconductor lattice-mismatched heteroepitaxial strained layers represent an important class of thin films in the development of high-performance electronic and optoelectronic devices. Strained epitaxy provides a means to combine materials whose electronic and optoelectronic properties can be tailored by composition and strain.[1] $Si_{1-x}Ge_x$ on Si and $Si_{1-y}C_y$ on Si are prototypical examples of such heteroepitaxial strained systems for which conventional transmission electron microscopy (TEM) has played an important role in characterizing the layer morphology and elucidating the mechanisms for strain relaxation in these systems.[2] However, one cannot easily distinguish between atomic species in heterostructures from the contrast in conventional high resolution TEM images. On the other hand, annular dark field scanning electron transmission microscopy (ADF-STEM) lattice images exhibit a strong elemental specificity because the image contrast depends strongly on the atomic number Z of the scattering atoms.[3,4] The technique thus offers additional analytical capabilities. The ADF-STEM image is known to depend on the average atomic number Z in a simple Z^n power-law relationship. For most microscope geometries, n is in the range of 1.6–1.9.[5] Unlike conventional high resolution TEM images, there is no contrast reversal with respect to defocus and sample thickness in high resolution high-angle ADF-STEM images.[6] The intensity maxima in the ADF-STEM image represent the actual atomic column position within the specimen; thus ADF-STEM images are more directly interpretable than conventional TEM images. Combined with electron energy loss spectroscopy (EELS), ADF-STEM imaging has become a widely used technique for crystallographic and chemical analyses at atomic resolution.[7]

The contrast of an ADF-STEM image has also been shown to depend on strain arising from point defects and dislocations,[8] or local lattice distortion at interfaces such as Si/SiO_2.[9] However, little work has been reported on the strain contrast in ADF-STEM imaging of heteroepitaxial strained layers. Recently, in a study of the strain contrast of dilute GaN_yAs_{1-y} ($y=0.029$ and 0.045) epitaxial layers on (100) GaAs, Wu *et al.*[10] observed that the dilute GaN_yAs_{1-y} strained films exhibited an unusual ADF-STEM image contrast. Contrary to the compositional contrast prediction of ADF-STEM image intensity, the lower average atomic number strained GaN_yAs_{1-y} layers were found to be brighter than the higher average atomic number GaAs for an ADF detector semiangle of up to 65 mrad in the 40 nm thick area of TEM samples. Applying multislice simulations it was shown that the displacement around substitutional N atoms was a determining factor for the observed ADF-STEM contrast and that the contribution to the contrast due to misfit strain between GaN_yAs_{1-y} and GaAs was small.[10] The thickness dependence of the ADF-STEM image contrast in heteroepitaxial strained films is another interesting question. Although it is widely accepted that there is no contrast reversal with respect to sample thickness in ADF-STEM images, strain contrast at an amorphous silicon/crystalline silicon interface is known to

[a]Electronic mail: xiaohua.wu@nrc.ca.

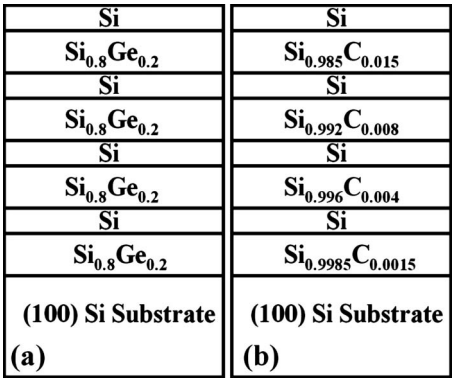

FIG. 1. Structures of samples (a) $Si_{1-x}Ge_x$ and (b) $Si_{1-y}C_y$.

exhibit a sample thickness dependence.[9] It is also well known that TEM samples from strained layers exhibit partial elastic strain relaxation that depends on the TEM sample thickness to the strained layer thickness ratio. To shed more light on the origin of ADF-STEM image contrast in strained films, we report a study of the ADF-STEM image contrast dependence on detector angle and TEM sample thickness in the heteroepitaxial strained films. For the present work, compressive strained $Si_{0.8}Ge_{0.2}$ layers and tensile strained dilute $Si_{1-y}C_y$ ($y \leq 0.015$) epitaxial layers grown on (100) Si substrates are studied in a STEM. A series of ADF images is obtained with detector inner semiangle ranging from 26 to 92 mrad, and sample thickness ranging from 50 to 330 nm. The contrast between the strained layers and Si substrate in high magnification ADF-STEM lattice images is compared with that in low magnification ADF-STEM images. The observed contrast of the ADF-STEM images is discussed in relation to the atomic scattering and modeled in multislice simulations. The intensity line profile of the ADF-STEM images is analyzed to obtain the composition profile in these thin strained layers and the results are compared with composition profiles obtained by analytical TEM techniques: energy dispersive x-ray spectroscopy (EDX) and EELS, as well as secondary ion mass spectrometry (SIMS).

II. EXPERIMENT

The structure of the two heterostructures used for this study is illustrated in Fig. 1. The first sample is a $Si/Si_{1-x}Ge_x$ epitaxial structure consisting of four 40 nm thick $Si_{0.8}Ge_{0.2}$ strained layers separated by 40 nm thick Si spacer layers. The second sample is a dilute $Si_{1-y}C_y$ staircase structure consisting of four $Si_{1-y}C_y$ individual strained layers of 30–60 nm thickness of increasing nominal composition ($y=0.0015$, 0.004, 0.008, and 0.015 from bottom to top) separated by 50 nm thick Si spacers. These samples were grown by Si molecular beam epitaxy (MBE) in which the Si and Ge fluxes were produced by electron beam evaporation of elemental sources, while the C flux was obtained by plasma-assisted dissociation of methane in an electron cyclotron resonance (ECR) source. Details on growth methodology have been reported elsewhere.[11,12] The average Ge concentrations in the $Si_{1-x}Ge_x$ layers and C concentrations in the $Si_{1-y}C_y$ layers were determined by high resolution x-ray diffraction (Bruker Discover D8), a technique which also confirmed that both structures were coherently stained. Details of composition depth profile were obtained by Auger electron spectroscopy (PHI 650) and SIMS (PHI Adept 1010) using calibration standards. ⟨011⟩ cross-sectional TEM samples were prepared following standard dimpling and ion milling procedures. A 200 kV JEOL JEM-2100F TEM/STEM equipped with an ultrahigh resolution pole piece ($C_s=0.5$ mm), a Fischione ADF detector (4–28 mm active diameter), a Gatan DigiScan, a Gatan imaging filter (GIF) Tridiem, and an Oxford INCA EDX was used for this study. The line scan intensity across the center of the Airy-shaped electron probe image displaces a Gaussian profile and the full width at half maximum was measured to be 0.18 nm.[10] With a 40 μm STEM objective aperture in the JEM-2100F (this corresponds to the conventional TEM condenser aperture), the probe convergence semiangle used in this study was measured to be 14.3 mrad, which is higher than the theoretical optimal semiangle of 10.7 mrad given by $1.27(\lambda/C_s)^{1/4}$ where λ is the wavelength of the incident electrons.[13] The ADF detector inner semiangles were calibrated by recording a ⟨011⟩ zone axis Si diffraction pattern and the shadow image of the inner edge of the ADF detector simultaneously in the GIF charge coupled device camera. The ADF detector inner semiangles used were 26, 29, 38, 42, 51, 67, 78, and 92 mrad and the outer collection semiangle was the maximum value of 175 mrad accessible on the JEOL JEM-2100F with ultrahigh resolution pole piece.[14] Care has been given to precisely adjust "gain" and "brightness" of the ADF detector in order to obtain accurate and meaningful intensity measurements.[15] The thickness of the various TEM cross-sectional samples was determined from the ratio of the plasmon to the zero-loss peaks in the electron energy loss spectrum.

III. OBSERVATIONS

A. $Si_{0.8}Ge_{0.2}$ sample

Figure 2(a) displays a low magnification ADF-STEM image of the $Si_{0.8}Ge_{0.2}$ sample, and Fig. 2(b) is a high magnification ADF-STEM lattice image from the $Si_{1-x}Ge_x/Si$ interface area indicated in Fig. 2(a). The thickness of the TEM sample at the area of Fig. 2(b) is about 105 nm. As expected, $Si_{0.8}Ge_{0.2}$ layers are much brighter than Si layers, consistent with a larger average atomic number in the $Si_{0.8}Ge_{0.2}$ layer (17.6) than in the surrounding Si layers (14). Figures 2(c) and 2(d) are high magnification ADF-STEM lattice images acquired in thicker regions of the same sample (thicknesses of 224 and 301 nm, respectively). With increasing sample thickness, the image resolution is preserved, but the signal to noise (S/N) level is reduced. This phenomenon, reported and discussed previously in other materials systems,[16,17] has been attributed to the increase in the effective electron probe size with increasing sample thickness leading to a loss of resolution and larger background.

In order to quantitatively compare the contrasts of $Si_{0.8}Ge_{0.2}$ relative to Si from low and high resolution ADF-STEM images, intensity line profiles were obtained using Gatan digital micrography. Figure 3 is an example of intensity line profiles from low and high magnification ADF-STEM images. The areas and directions of intensity line pro-

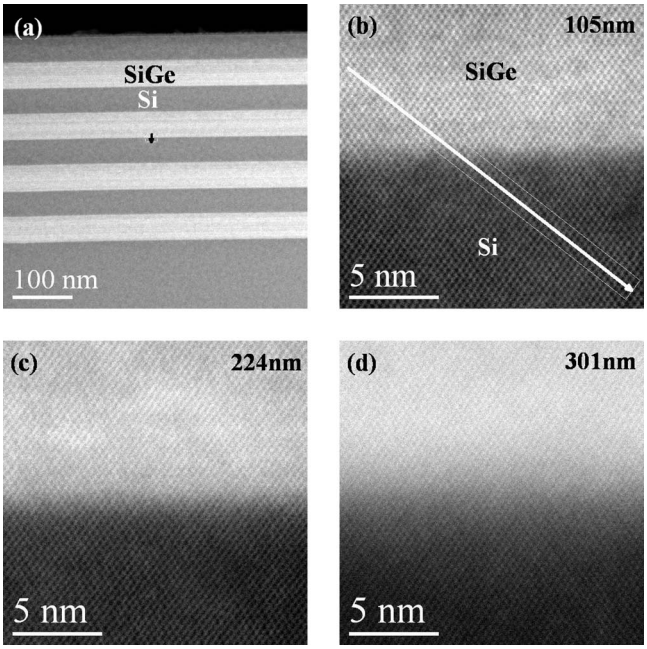

FIG. 2. Low and high resolution ADF-STEM images of the $Si_{1-x}Ge_x$ sample obtained at 42 mrad ADF detector inner semiangle. The TEM sample thicknesses are indicated in the images. Note that (b) is the enlargement of the square area with an arrow.

files are indicated in Figs. 2(a) and 2(b). The intensity line profile was integrated over a width of 19.8 nm and along ⟨100⟩ direction for the low magnification ADF-STEM image

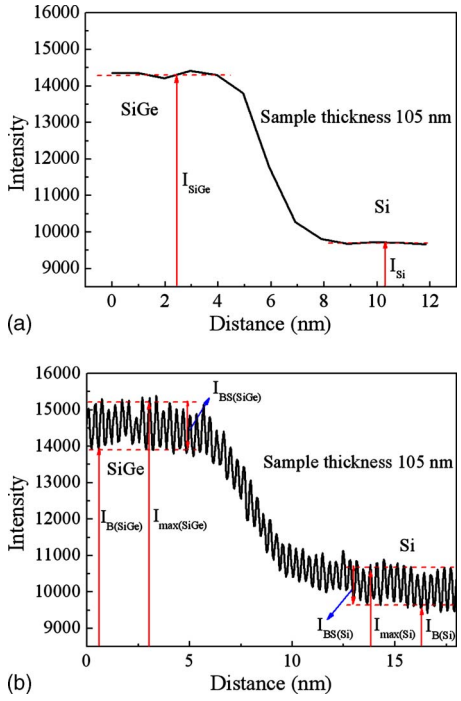

FIG. 3. (Color online) Intensity line profiles of low and high resolution ADF-STEM images of Figs. 2(a) and 2(b). I_X is the intensity obtained from the low magnification ADF-STEM images, where X is either $Si_{1-x}Ge_x$ or Si. $I_{max(X)}$ is the mean value of the maximum intensity of a high magnification ADF-STEM lattice image, which is measured on the ⟨111⟩ atomic columns. $I_{B(X)}$ is the mean value of the intensity of the background, which is measured between the ⟨111⟩ atomic columns. The background subtracted column intensity $I_{BS(X)}$ is given by $I_{BS(X)}=I_{max(X)}-I_{B(X)}$.

TABLE I. Various intensity ratios of $Si_{1-x}Ge_x$ to Si measured from low and high resolution ADF-STEM images.

TEM sample thickness (nm)	I_{SiGe}/I_{Si}	$I_{max(SiGe)}/I_{max(Si)}$	$I_{B(SiGe)}/I_{B(Si)}$	$I_{BS(SiGe)}/I_{BS(Si)}$
73	1.49	1.48	1.48	1.40
105	1.45	1.44	1.44	1.37
145	1.43	1.44	1.46	1.09
224	1.43	1.43	1.45	1
301	1.40	1.40	1.42	0.82

[Fig. 2(a)], and over a width of 1.32 nm and along ⟨111⟩ direction for the high magnification ADF-STEM lattice image [Fig. 2(b)]. As shown in Fig. 3(a), we denote as I_X the intensity obtained from the low magnification ADF-STEM images, where X is either $Si_{1-x}Ge_x$ or Si. Also indicated in Fig. 3(b), $I_{max(X)}$ is the mean value of the maximum intensity of an ADF-STEM lattice image, which is measured on the ⟨111⟩ atomic columns, $I_{B(X)}$ is the mean value of the intensity of the background, which is measured between the ⟨111⟩ atomic columns. The background subtracted column intensity $I_{BS(X)}$ is given by $I_{BS(X)}=I_{max(X)}-I_{B(X)}$.

Table I summarizes the various measured intensity ratios between $Si_{1-x}Ge_x$ and Si (I_{SiGe}/I_{Si}, $I_{max(SiGe)}/I_{max(Si)}$, $I_{B(SiGe)}/I_{B(Si)}$, and $I_{BS(SiGe)}/I_{BS(Si)}$) for different TEM sample thicknesses. The intensity ratios (and, thus, contrast between $Si_{1-x}Ge_x$ and Si) from low resolution ADF-STEM images (I_{SiGe}/I_{Si}) are very close to the ratios from high resolution ADF-STEM images when the mean values of the maximum intensity measured along the ⟨111⟩ atomic columns ($I_{max(SiGe)}/I_{max(Si)}$) or the mean values of the background intensity measured between the ⟨111⟩ atomic columns ($I_{B(SiGe)}/I_{B(Si)}$) are used. A closer look at the data from Table I however reveals that $I_{max(SiGe)}/I_{max(Si)}$ is closer to I_{SiGe}/I_{Si} than $I_{B(SiGe)}/I_{B(Si)}$. Thus, the intensity of low resolution ADF-STEM images represents the mean value of the maximum intensity measured on the atomic columns of the high resolution ADF-STEM lattice images. In contrast the background subtracted intensity ratio ($I_{BS(SiGe)}/I_{BS(Si)}$) exhibits a peculiar trend as a function of sample thickness. When the sample thickness is less than 100 nm, the background subtracted intensity ratio ($I_{BS(SiGe)}/I_{BS(Si)}$) is close to other intensity ratios (I_{SiGe}/I_{Si}, $I_{max(SiGe)}/I_{max(Si)}$, and $I_{B(SiGe)}/I_{B(Si)}$), but a significant departure is seen when the sample thickness exceeds 100 nm. As shown in Figs. 2(b)–2(d), the high resolution ADF-STEM image S/N level reduces as the sample thickness increases. This means that $I_{max(x)}/I_{B(x)}$ decreases with increasing sample thickness. Figure 4 presents the plot of the absolute background subtracted intensity ($I_{BS(X)}$) as a function of sample thickness for both $Si_{1-x}Ge_x$ and Si. An interesting observation is that with increasing thickness, $I_{BS(SiGe)}$ decreases more rapidly than $I_{BS(Si)}$. $I_{BS(X)}$ represents the contrast between the atomic column and its background, which depends on the spatial distribution of the electron probe. This implies that any change in the probe shape traveling through the sample will affect $I_{BS(X)}$.[18] The lattice of strained

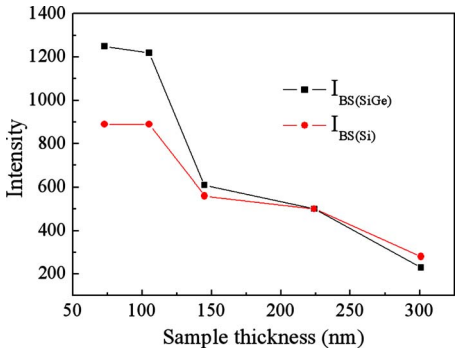

FIG. 4. (Color online) Background subtracted intensity $I_{BS(X)}$ vs sample thickness for the $Si_{1-x}Ge_x$/Si heterostructure.

$Si_{1-x}Ge_x$ is distorted because of the misfit strain, and this distortion is small in very thin samples due to the strain relaxation of TEM samples. But the degree of distortion increases with increasing sample thickness within few hundreds of nanometers, which likely leads to more rapid decrease in $I_{BS(SiGe)}$ than $I_{BS(Si)}$.

The contrast (C) between $Si_{1-x}Ge_x$ and Si defined as

$$C = (I_{SiGe}/I_{Si}) - 1 \quad (1)$$

varies in the range of $0.40 < C < 0.49$ for this $Si_{1-x}Ge_x$/Si sample (see Table I). The Z contrast is expected to follow a relationship of the form $C = (Z_{SiGe}/Z_{Si})^n - 1$ corresponding to contrasts of 0.44 and 0.54 when $n = 1.6$ and 1.9, respectively.[5] Because the low magnification ADF-STEM images can accurately reflect the contrast between $Si_{1-x}Ge_x$ and Si, all intensities used for the contrast calculation are from low magnification ADF-STEM images unless otherwise stated. An example of the intensity profile obtained from Eq. (1) is shown in Fig. 5. The intensity line profile [Fig. 5(b)] was integrated over a width of 100 nm along a ⟨100⟩ direction as shown in Fig. 5(a). The intensity profile exhibits short range fluctuations in the $Si_{1-x}Ge_x$ layers and is fairly uniform in the Si spacers. The former oscillations point to presence of variations in the Ge concentration in the growth direction and will be further discussed below.

Figure 6 compares the evolution of contrast with sample thickness for six different ADF detector semiangles. The intensity of $Si_{1-x}Ge_x$ (I_{SiGe}) was obtained from the average of four $Si_{1-x}Ge_x$ layers [SiGe1, SiGe2, SiGe3, and SiGe4 in Fig. 5(a)], and that of Si (I_{Si}) from the average of three Si spacer layers [Si1, Si2, and Si3 in Fig. 5(a)]. In all cases the following trend is observed: monotonic decrease in the contrast with sample thickness from 50 nm to about 120 nm and almost constant contrast for samples of thickness exceeding 120 nm. The loss of contrast with increasing thickness is concomitant with a decrease in thin foil strain relaxation effects as the sample thickness increases.[19] It has been shown that strain relaxation in thin TEM samples is localized only near the free surface when the sample thickness is three times thicker than the strained layer thickness.[20,21] With $Si_{1-x}Ge_x$ layers of 40 nm thickness, the strain retained in individual $Si_{1-x}Ge_x$ layer within the TEM sample of thickness exceeding ~120 nm will be the same. For sample thickness less than 120 nm, less misfit strain within the

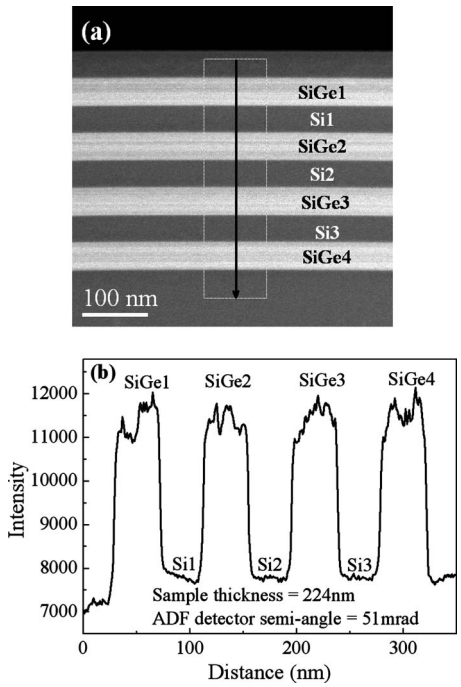

FIG. 5. Measurement of ADF-STEM image intensities of the $Si_{1-x}Ge_x$/Si heterostructure. (a) An ADF-STEM image taken with 51 mrad ADF detector inner semiangle and sample thickness of 224 nm. (b) The intensity line profile from image (a).

$Si_{1-x}Ge_x$ layers in the thinner area leads to higher contrast between $Si_{1-x}Ge_x$ and Si as compared to $Si_{1-x}Ge_x$ layers in thicker areas. Thus, the misfit strain in the $Si_{1-x}Ge_x$ layers reduces its ADF-STEM intensity, and contributes negatively to the ADF-STEM image contrast between $Si_{1-x}Ge_x$ and Si. When the thickness is greater than 120 nm, most of the misfit strain in the $Si_{1-x}Ge_x$ layers is retained and the misfit strain in $Si_{1-x}Ge_x$ layers is the same. The contrast between the $Si_{1-x}Ge_x$ and Si is then independent of the sample thickness.

Another important observation from Fig. 6 is that for a given thickness, the contrast increases with the increase in the ADF detector semiangle. The dependence of the contrast on ADF detector semiangle is further discussed in Sec. IV.

B. $Si_{1-y}C_y$ sample

Figures 7 and 8 show two groups of ⟨011⟩ zone axis ADF-STEM images of the $Si_{1-y}C_y$ sample taken at detector

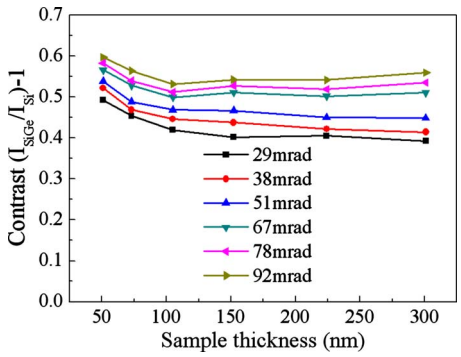

FIG. 6. (Color online) Variation in the contrast with TEM sample thickness at various ADF detector semiangles for the $Si_{1-x}Ge_x$ on Si heterostructure.

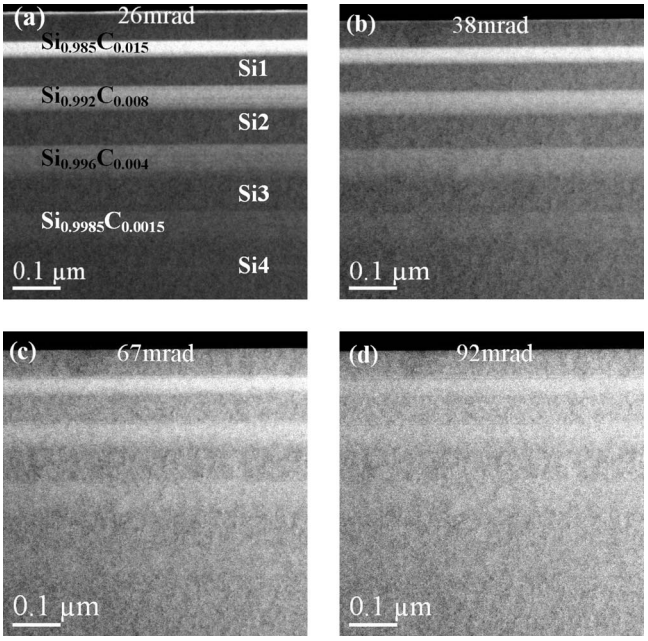

FIG. 7. ADF-STEM images acquired at four different detector angles in a TEM sample of 330 nm thickness.

inner-outer semiangles of 26-175, 38-175, 67-175, and 92-175 mrad. The thicknesses of the samples at the center of the image are 330 nm (Fig. 7) and 135 nm (Fig. 8). For the 330 nm thick sample, it is observed that there is a large intensity difference between the $Si_{1-y}C_y$ and Si layers at lower detector inner semiangles, which is less pronounced at larger semiangles. Contrary to the compositional contrast prediction of ADF-STEM imaging, the lower average atomic number $Si_{1-y}C_y$ layers are brighter than the surrounding higher average atomic number Si for the ADF detector semiangle of up to 92 mrad (Fig. 7). The systematic increase in intensity

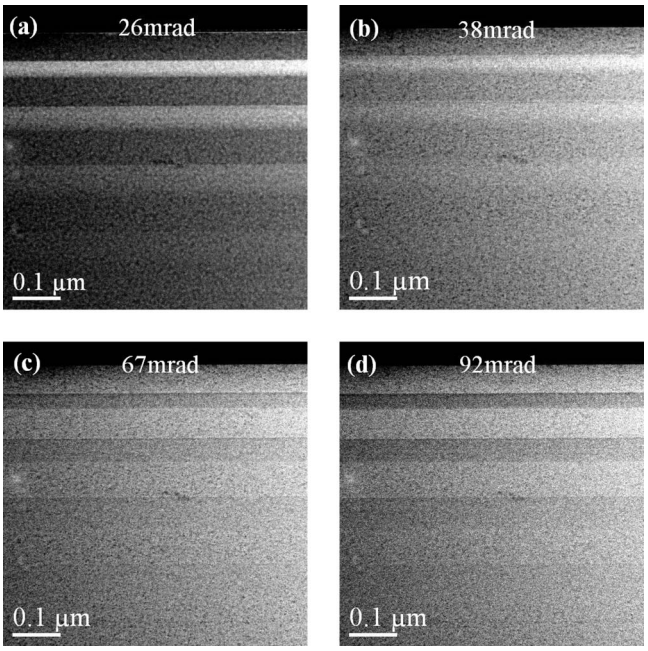

FIG. 8. ADF-STEM images acquired at four different detector angles in a TEM sample of 135 nm thickness.

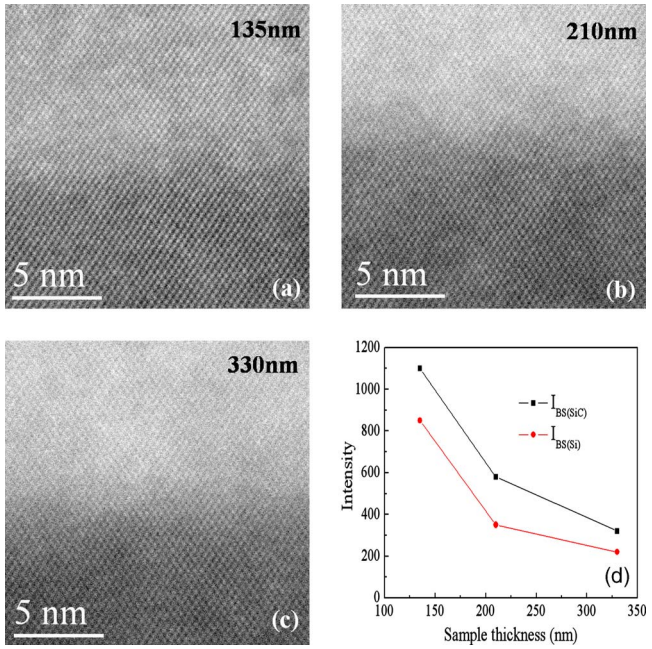

FIG. 9. (Color online) [(a)–(c)] High resolution ADF-STEM images of the $Si_{1-y}C_y$ sample obtained at 42 mrad ADF detector inner semiangle. The thicknesses are indicated in the images. (d) Background subtracted intensity $I_{BS(X)}$ vs sample thickness for $Si_{1-y}C_y/Si$.

from left to right in all of the images is due to increasing specimen thickness along that direction. For the 135 nm thick sample (Fig. 8), this anomalous contrast between $Si_{1-y}C_y$ and Si noted in the 330 nm thick sample is also observed for the ADF detector semiangles of 26 and 38 mrad [Figs. 8(a) and 8(b)]. However, the normal ADF-STEM Z contrast between $Si_{1-y}C_y$ and Si is obtained with the ADF detector semiangles of 67 and 92 mrad [Figs. 8(c) and 8(d)].

The low and high magnification ADF-STEM images of the $Si_{1-y}C_y$ sample show similar characteristics as the $Si_{1-x}Ge_x$ sample. The intensity of low magnification ADF-STEM images represents the mean values of the maximum intensity measured on the atomic columns of the high resolution ADF-STEM lattice images. For the high magnification lattice images, the S/N level decreases as the sample thickness increases, but the image resolution is preserved [Figs. 9(a)–9(c)]. However, the background subtracted intensity $I_{BS(X)}$ of $Si_{1-y}C_y$ on Si [Fig. 9(d)] shows an opposite trend to that of the $Si_{1-x}Ge_x$ on Si system in that although $I_{BS(X)}$ decreases with increasing sample thickness as expected, $I_{BS(SiC)}$ is greater than $I_{BS(Si)}$ in all thickness regions where the images were obtained. An example of the contrast measurement for the $Si_{1-y}C_y$ sample is shown in Fig. 10. Here the intensity line profile [Fig. 10(b)] was integrated over a width of 0.48 μm and along $\langle 100 \rangle$ direction as shown in Fig. 10(a).

Figure 11 presents plots of the contrast dependence on sample thickness for various ADF detector semiangles for the $Si_{1-y}C_y$ sample. The dependence of the contrast on the sample thickness is different from that observed in the $Si_{1-x}Ge_x$ sample: the contrast increases with increasing sample thickness in the 50–200 nm range and remains almost constant in thicker samples. The contrast dependence on the ADF detector semiangle also shows an opposite trend with

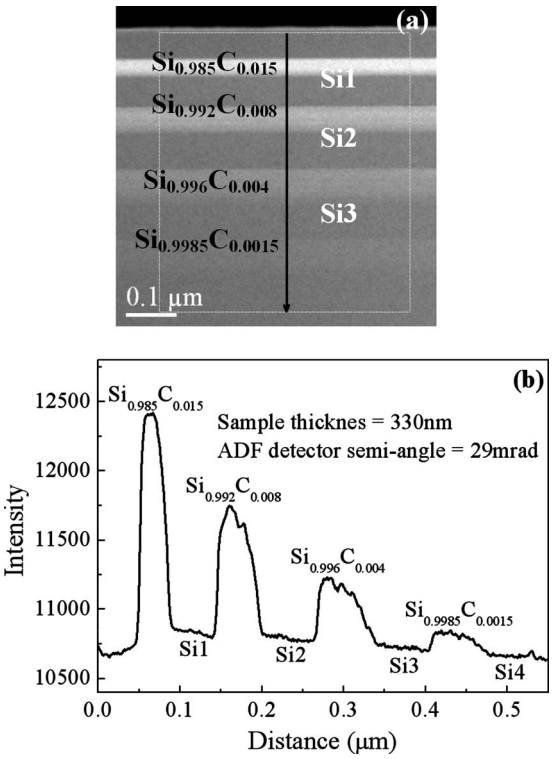

FIG. 10. Measurement of ADF-STEM image intensities of $Si_{1-y}C_y$ and Si. (a) An ADF-STEM image taken with 29 mrad ADF detector inner semiangle and sample thickness of 330 nm. (b) The intensity line profile from image (a).

the contrast decreasing as the ADF detector semiangle is increased. To better appreciate the dependence of the contrast on the ADF detector semiangle, the data shown in Fig. 11 were replotted in Fig. 12 as the contrast variation as a function of ADF detector semiangle at various sample thickness. For samples with thicknesses of 89 and 135 nm [Figs. 12(a) and 12(b)], the contrast between $Si_{1-y}C_y$ and Si goes from positive to negative as the ADF detector semiangle increases

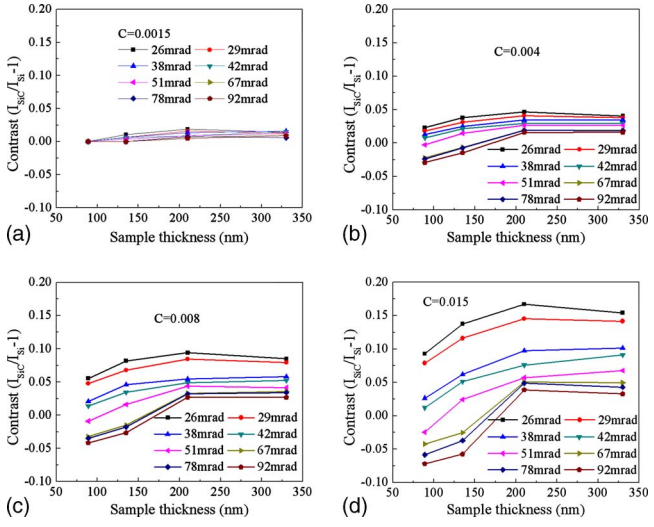

FIG. 11. (Color online) Evolution of the ADF-STEM image contrast with TEM sample thickness at various ADF detector semiangles for (a) $Si_{0.9985}C_{0.0015}/Si$, (b) $Si_{0.996}C_{0.004}/Si$, (c) $Si_{0.992}C_{0.008}/Si$, and (d) $Si_{0.985}C_{0.015}/Si$.

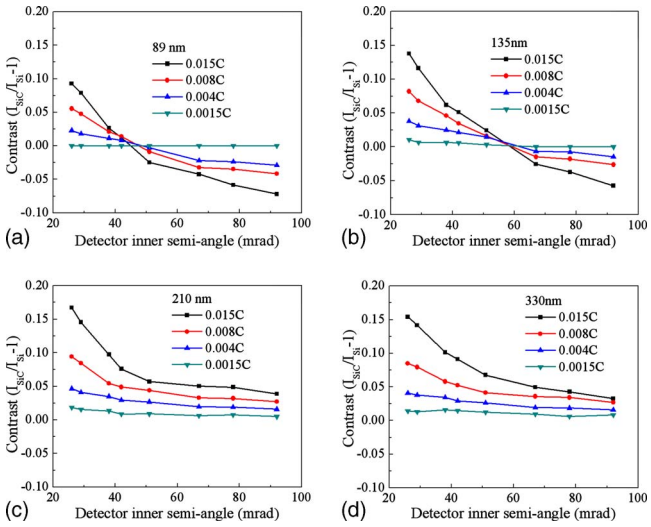

FIG. 12. (Color online) Evolution of the ADF-STEM image contrast with. ADF detector semiangles for different C concentrations at (a) 89, (b) 135, (c) 210, and (d) 330 nm.

(this is also seen in Fig. 8). The contrast is exclusively positive for samples with thicknesses of 210 and 330 nm [Figs. 12(c) and 12(d)] as seen in Fig. 7.

IV. DISCUSSION

The $Si_{1-x}Ge_x/Si$ and $Si_{1-y}C_y/Si$ systems exhibit opposite ADF-STEM image contrast dependences on the ADF-STEM detector collection angles: the contrast increases with increasing ADF detector angle for $Si_{1-x}Ge_x/Si$ (Fig. 6), while it decreases with increasing ADF detector angle for $Si_{1-y}C_y/Si$ (Figs. 11 and 12). For the $Si_{1-y}C_y/Si$ system, a unique contrast dependence on TEM sample thickness was observed (Figs. 7 and 8). Table II summarizes some of the relevant material properties for the two samples $Si_{0.8}Ge_{0.2}$ and $Si_{0.985}C_{0.015}$, which are used in the discussion that follows. Here we use the highest C concentration $Si_{0.985}C_{0.015}$ layer to discuss $Si_{1-y}C_y$ sample. The lattice constant of $Si_{1-x}Ge_x$ is obtained form the expression $a_{Si_{1-x}Ge_x}=a_{Si}+0.0214x+0.001\,05x^2$ nm,[22] while that of $Si_{1-y}C_y$ is calculated following the equation $a_{Si_{1-y}C_y}=a_{Si}-0.242\,39y+0.057\,05y^2$ nm.[23] Other physical parameters for $Si_{1-x}Ge_x$ and $Si_{1-y}C_y$ films have been estimated from the data for elemental Si and Ge and C, using Vegard's law, e.g., any physical parameter of an alloy is approximated by a linear interpolation of the bulk value of its constituents.

For heteroepitaxial growth of $Si_{1-x}Ge_x$ or $Si_{1-y}C_y$ films on a (100) Si substrate, there is a misfit strain due to the difference in lattice constants between the films and substrates. Since the Si substrates are much thicker than $Si_{1-x}Ge_x$ or $Si_{1-y}C_y$ layers, all the strain is assumed to be confined to the epitaxial $Si_{1-x}Ge_x$ or $Si_{1-y}C_y$ layers. Since the lattice constant of $Si_{1-x}Ge_x$ ($Si_{1-y}C_y$) is greater (smaller) than that of Si (Table II), the $Si_{1-x}Ge_x$ ($Si_{1-y}C_y$) films are under biaxial compressive (tensile) stress, resulting in the tetragonal distortion of the $Si_{1-x}Ge_x$ ($Si_{1-y}C_y$) lattice. Here we define a coordinate system in which the y-axis is parallel to the (100) growth direction and the plane containing the x- and z-axes is parallel to the film-substrate interface plane. After

TABLE II. Properties of $Si_{0.8}Ge_{0.2}$ and $Si_{0.985}C_{0.015}$.

	Si	Ge	C	$Si_{0.8}Ge_{0.2}$	$Si_{0.985}C_{0.015}$
Lattice constant a (nm) (before epitaxy)	0.5431	0.5658	3.567	0.5474	0.5395
Misfit strain displacement (nm)	0			−0.0043	0.0036
Lattice misfit f (%)	0			−0.83	0.66
Average atomic number	14	32	6	17.6	13.88
Poisson's ratio ν	0.28	0.26	0.10	0.28	0.28
Elemental radius (nm)	0.120	0.117	0.068		
Amplitude of thermal vibration at room temperature u_T (nm)	0.0078	0.009	0.005	0.008	0.0078

the epitaxial growth, the lattice parameters of Si remain at the bulk values of $a=b=c=0.5431$ nm. For the strained $Si_{1-x}Ge_x$ and $Si_{1-y}C_y$ films, the in-plane lattice parameters are constrained to match the substrates values, $a=c=0.5431$ nm, so the strain displacement along x and z directions is $0.5474-0.5431=0.0043$ nm for $Si_{1-x}Ge_x$ and $0.5395-0.5431=-0.0036$ nm for $Si_{1-y}C_y$. From linear elasticity theory, the perpendicular lattice constant of the film, b, is given by $\{1-[2\nu/(1-\nu)]f\}a$ and has a greater value $b=0.5511$ nm for $Si_{1-x}Ge_x$ and a smaller value $b=0.5367$ nm for $Si_{1-y}C_y$ film. For defect-free crystals, the ADF-STEM image intensity can be fully accounted for by elastic scattering and thermal diffuse scattering (TDS).[24] The differential cross sections for elastic scattering and TDS are given by[25,26]

$$\left[\frac{d\sigma(\theta)}{d\Omega}\right]_{\text{Elastic}} = \frac{4\gamma^2 Z^2}{a_0^2 k_0^4}\frac{1}{(\theta^2+\theta_0^2)^2}\{\exp[-2(M^T)\theta^2]\}, \quad (2)$$

$$\left[\frac{d\sigma(\theta)}{d\Omega}\right]_{\text{TDS}} = \frac{4\gamma^2 Z^2}{a_0^2 k_0^4}\frac{1}{(\theta^2+\theta_0^2)^2}\{1-\exp[-2(M^T)\theta^2]\}, \quad (3)$$

where $\theta_0=(k_0 r_0)^{-1}$ is the characteristic angle of elastic scattering, $k_0=2505$ nm^{-1} is the wave vector (at 200 keV), $r_0=a_0 Z^{-1/3}$ is a screening radius, $a_0=0.0529$ nm is the first Bohr radius, $\gamma=1.394$ (at 200 keV) is a relativistic factor, and Z is the average atomic number. $M^T=8\pi^2 u_T^2/\lambda^2$ is the Debye–Waller factor and u_T is the amplitude of thermal vibration.

The scattering of the incident electrons from a random strain field can be treated similarly to that from TDS, and an extra Debye–Waller factor can be added to the cross section of TDS to account for the strain effect:[10]

$$\left[\frac{d\sigma(\theta)}{d\Omega}\right]_{\text{TDS+Strain}} = \frac{4\gamma^2 Z^2}{a_0^2 k_0^4}\frac{1}{(\theta^2+\theta_0^2)^2}\{1-\exp[-2(M^T+M^S)\theta^2]\}, \quad (4)$$

where $M^S=8\pi^2 u_S^2/\lambda^2$ and u_S is the amplitude of the strain.

Figure 13 shows plots of $[d\sigma(\theta)/d\Omega]$ as a function of θ for Si, $Si_{1-x}Ge_x$, and $Si_{1-y}C_y$ using Eqs. (2)–(4). Insets of Figs. 13(a) and 13(b) are rescaled plots for showing the cross section differences between Si and $Si_{1-x}Ge_x$, and between Si and $Si_{1-y}C_y$ at high scattering angle θ. At high θ, TDS (for Si) or TDS plus strain (for $Si_{1-x}Ge_x$ and $Si_{1-y}C_y$) dominates the ADF-STEM image intensity. For the $Si_{1-x}Ge_x$ sample, the cross section of $Si_{1-x}Ge_x$ is always greater than that of Si mainly due to the higher $Si_{1-x}Ge_x$ atomic number. In other words, composition plays a crucial role in ADF-STEM image contrast for the $Si_{1-x}Ge_x$ sample. In the $Si_{1-y}C_y$ sample,

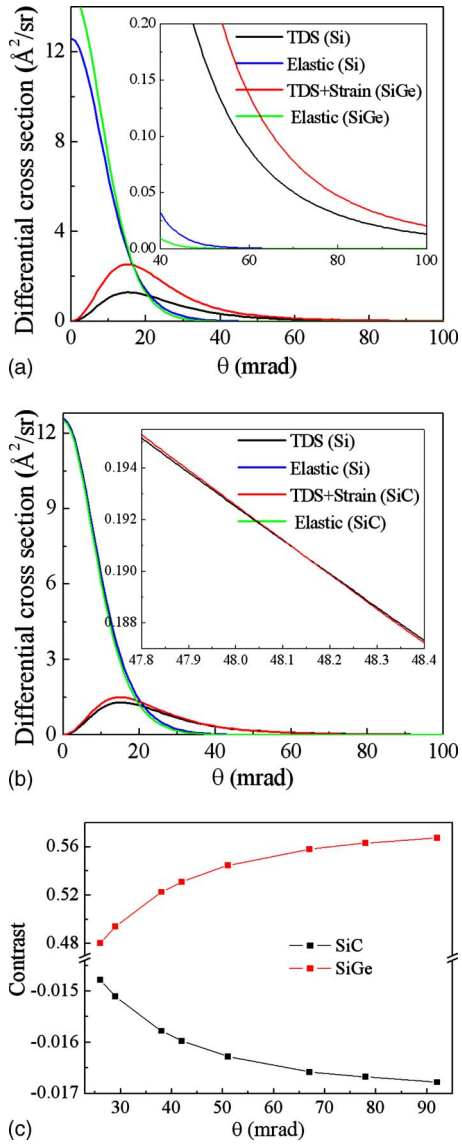

FIG. 13. (Color online) Variation in the scattering cross section with the scattering angle of elastic scattering, TDS, and TDS with strain for (a) $Si_{0.8}Ge_{0.2}/Si$ and (b) $Si_{0.985}C_{0.015}/Si$. Panel (c) shows the dependence of contrast on scattering angle calculated from (a) and (b) for $Si_{0.8}Ge_{0.2}/Si$ and $Si_{0.985}C_{0.015}/Si$.

the average atomic number for the highest C concentration layer $Si_{0.985}C_{0.015}$ is 13.88 (see Table II), and very close to 14 of Si. In this case, the angular distribution term [the term in the square parentheses in Eqs. (3) and (4)] plays a very significant role in the ADF-STEM image intensity. It is observed from the inset of Fig. 13(b) that the cross section of $Si_{1-y}C_y$ is greater than that of Si only when $\theta < 48.1$ mrad.

To understand the observed opposite dependences of the contrast on the ADF detector angle for the $Si_{1-x}Ge_x/Si$ and $Si_{1-y}C_y/Si$ systems, the intensity collected by the ADF detector was calculated by integrating the cross section over the detector geometry. Note that the total intensity of an ADF-STEM image arises from both elastic, TDS and strain (if any), and therefore the cross section of elastic scattering should be included in the calculation (its contribution is particularly important in the low ADF detector angle range). Figure 13(c) shows general agreement of the contrast dependence on ADF detector angle with experimental observations: for $Si_{1-x}Ge_x/Si$, the contrast increases with increasing ADF detector angle, while the contrast decreases with the increase in ADF detector angle for $Si_{1-y}C_y/Si$. The simple atomic scattering model explains the general trends observed in the ADF-STEM imaging contrast for epitaxial strained $Si_{1-x}Ge_x$ and $Si_{1-y}C_y$ on (001) Si. However, it should be noted that the differential cross section applies to a single atom, and neglects some experimental factors that contribute to the ADF-STEM image intensity such as sample thickness, beam convergence angle, probe size, and multiple electron scattering effects. Nevertheless, the single atomic scattering is the basis of accurate multislice calculation, and this simple approach agrees with the observed dependence of ADF-STEM image contrast on detector semiangle for both $Si_{1-x}Ge_x/Si$ and $Si_{1-y}C_y/Si$ systems.

To understand the different ADF-STEM image contrast dependences on sample thickness in the $Si_{1-y}C_y$ sample (Figs. 7 and 8), multislice calculations were performed following earlier work on the dilute GaNAs/GaAs system.[10] In multislice calculations, the sample thin foil is divided into a series of thin lamellas and the electron beam is propagated sequentially through each layer. The ADF-STEM image intensity is obtained by integrating the intensity of the convergent beam electron diffraction pattern over the range of inner and outer semiangles of the detector for each pixel in the image. For the GaNAs/GaAs system, the displacement around substitutional N atoms was found to play a critical role in determining the ADF-STEM contrast between dilute GaNAs and GaAs. Likewise, the lattice misfit strain in the dilute $Si_{1-y}C_y/Si$ system gives the average effects of strain over a large volume. On an atomic scale however, there are local variations in the strain arising from radial displacements around substitutional C atoms in the $Si_{1-y}C_y$ lattice because the C atomic radius of 0.068 nm is much smaller than the 0.120 nm atomic radius of the Si host atoms. For $Si_{1-x}Ge_x$ lattice, this local variation in the strain is very small because of the similar atomic radii of Ge (0.117 nm) and Si. The displacement ($\boldsymbol{u}$) of the atoms surrounding each substitutional Si atom in $Si_{1-y}C_y$ due to the atomic radius difference between Si and C atoms can be modeled using linear elasticity theory in the isotropic approximation as

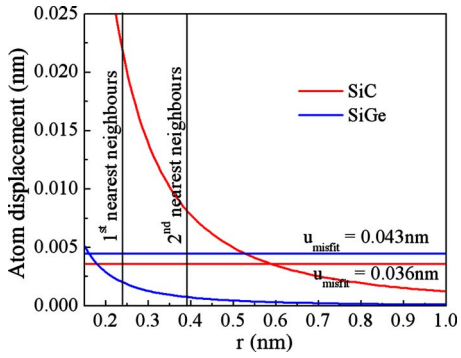

FIG. 14. (Color online) Comparison of the displacement around a substitutional C and Ge atom with lattice misfit displacement in $Si_{0.985}C_{0.015}$ and $Si_{0.8}Ge_{0.2}$.

$$\boldsymbol{u} = (c/r^3)\boldsymbol{r}, \tag{5}$$

where c is a constant dependent on the degree of lattice distortion around the C atoms and $\mathbf{r}$ is a position vector in the lattice. A value for c can be estimated from elasticity theory,[27]

$$\frac{da}{a} = 4\pi\frac{1-\nu}{1+\nu}\frac{yc}{\Omega}, \tag{6}$$

where y is the C concentration, $\nu = 0.28$ is Poisson's ratio for Si, da/a is a measure of the lattice misfit with $da = a_{Si} - a_{Si_{1-y}C_y} = 0.0036$ nm, and $\Omega = 20.02 \times 10^{-3}$ nm^3 is the volume per atom in the lattice. Substituting these values into Eq. (6) gives $c = 1.25 \times 10^{-3}$ nm^3. The magnitude of the atomic displacements predicted using Eqs. (5) and (6) is plotted in Fig. 14 and it is observed that for the first and second nearest neighbor atoms (0.2352 and 0.3843 nm, respectively) the displacements are significantly greater than those arising from uniform lattice misfit strain. Also included in Fig. 14 is comparison of uniform misfit strain and local displacement around Si for $Si_{1-x}Ge_x$. The displacement is negligible for $Si_{1-x}Ge_x$ as expected.

In the multislice simulation, carbon was incorporated into the $Si_{0.985}C_{0.015}$ layer by first randomly substituting 1.5% of the Si atoms with C atoms and then displacing the atoms in the lattice to account for the strain around the C atoms. Figure 15 compares multislice simulation results for Si and $Si_{1-y}C_y$ intensity in ADF-STEM images for various scattering angles θ for two different sample thicknesses of (a) 134.4 and (b) 326.4 nm. For 134.4 nm thick sample, the strained $Si_{1-y}C_y$ scatters more intensity than Si for $\theta < \sim 50$ mrad, and scatters less intensity than Si for $\theta > \sim 50$ mrad, which is in agreement with the experimental observations in the 135 nm thick sample as shown in Fig. 8: the $Si_{1-y}C_y$ is brighter than Si when ADF detector semiangles are 26 and 38 mrad, but darker than Si when ADF detector semiangles are 67 and 92 mrad. For the 326.4 nm thickness sample, the multislice simulation predicts that $Si_{1-y}C_y$ should scatter more intensity than Si for all θ values, which again agrees with the experimental observations in the 330 nm thick sample as shown in Fig. 7: the $Si_{1-y}C_y$ is brighter than Si when ADF detector semiangles are 26, 38, 67, and 92 mrad.

Finally, like the contrast dependence on the ADF detector collection angle, the $Si_{1-x}Ge_x/Si$ and $Si_{1-y}C_y/Si$ systems

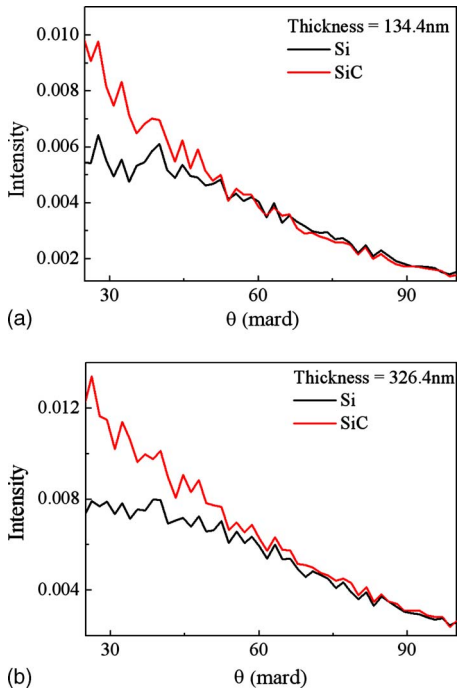

FIG. 15. (Color online) Multislice calculation of the intensity for Si and $Si_{1-y}C_y$ layers for TEM sample thicknesses of (a) 134.4 and (b) 326.4 nm.

also exhibit opposite ADF-STEM image contrast dependences on TEM sample thickness in relatively thin sample areas: the contrast decreases with increasing thickness for sample thickness less than ~120 nm for $Si_{1-x}Ge_x$ system (Fig. 6), while the contrast increases with increasing thickness for sample thickness less than ~200 nm for $Si_{1-y}C_y/Si$ system (Fig. 11). In the relatively thick sample areas, the contrast is independent of sample thickness for both $Si_{1-x}Ge_x/Si$ and $Si_{1-y}C_y/Si$ systems. The contrast dependence on the TEM sample thickness is likely related to the facts that composition plays a crucial role in ADF-STEM image contrast for the $Si_{1-x}Ge_x/Si$ system, and strain displacement around substitutional C atoms play a critical role in determining the ADF-STEM contrast in $Si_{1-y}C_y/Si$ system. Further theoretical works need to be done to fully understand the contrast dependence on TEM sample thickness for heteroepitaxial films.

V. APPLICATIONS

ADF-STEM imaging combined with EDX and EELS allows the simultaneous characterization of crystal morphology, structure, and composition in a STEM. Here both EDX and EELS could determine the Si and Ge compositions in the $Si_{0.8}Ge_{0.2}$ sample, but failed to determine C in the $Si_{1-y}C_y$ sample because of a C concentration below detection limit. Figure 16 compares Ge compositions obtained by EDX and EELS to the ADF-STEM image line profile of Fig. 5(b). In order to ease comparison of the composition profiles, the EDX and EELS Ge composition curves were moved up by 10% and 20%, respectively, while the ADF-STEM intensity line profile was adjusted so that average Si intensity coincides with zero, and the average $Si_{1-x}Ge_x$ intensity was set to 20%. The similarity of the Ge composition profiles measured

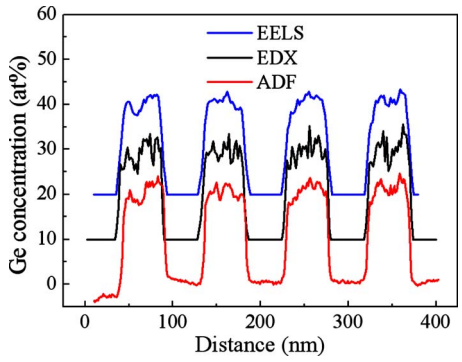

FIG. 16. (Color online) Comparison of Ge composition profiles obtained from EDX and EELS with the ADF-STEM image intensity line profile.

by the EDX or EELS and the ADF-STEM image contrast profile is striking. The local variations in the ADF-STEM contrast is clearly correlated with fluctuations in the Ge content within the films detected with the other analytical techniques and arising from Ge atomic flux instabilities during deposition. Furthermore, the magnitude of the ADF-STEM contrast variations scales precisely with the Ge content variations as determined by the analytical techniques. This shows that for this materials system, ADF-STEM image contrast analysis can be an accurate alternative method for evaluating material composition fluctuations in thin alloy heterostructures.

In the $Si_{1-y}C_y/Si$ system, despite the fact that the C concentration was beyond the detection limit of both EDS and EELS, a strong contrast between Si and $Si_{1-y}C_y$ layers was observed in certain ADF-STEM images. (See, for example, an ADF-STEM image acquired at 29 mrad detector semiangle and 330 nm sample thickness [Fig. 10(b)].) To verify whether or not this contrast can be correlated with the C composition of the layers, the C composition profile of the $Si_{1-y}C_y$ sample was obtained by SIMS. Figure 17 is the comparison of C composition as obtained by SIMS with the ADF-STEM image line intensity profile shown in Fig. 10(b). By adjusting the $Si_{0.985}C_{0.015}$ layer ADF-STEM image intensity to a 1.5 at. % C peak concentration, the C composition profiles as determined by SIMS coincide remarkably well with the ADF-STEM image line intensity profile for all four $Si_{1-y}C_y$ layers. In conjunction with another analytical technique such as SIMS or x-ray diffraction, the ADF-STEM image line intensity profile of dilute $Si_{1-y}C_y/Si$ system may

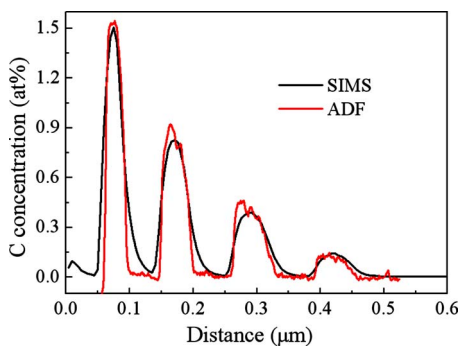

FIG. 17. (Color online) Comparison of the C composition profile as obtained from SIMS with the ADF-STEM image intensity line profile.

thus provide a means to estimate C concentration variation in the $Si_{1-y}C_y/Si$ system at concentrations beyond the detection limit of either EDX-STEM or EELS-STEM. In fact, details of the STEM-ADF C concentration profile in Fig. 17 may be linked to experimental conditions prevailing during the MBE deposition of the $Si/Si_{1-y}C_y$ staircase structure. For example, the slow increase in C content from the bottom to top in the more dilute layers may be correlated with transients and stabilization periods of the ECR plasma C source. Instabilities in the ECR source may also have caused local C composition variations that are revealed by spikes in the ADF-STEM profile, but that could not be resolved by SIMS. Also, ADF-STEM exhibits a better depth resolution than SIMS and reveals that the $Si/Si_{1-y}C_y$ interfaces chemically sharper than what SIMS would suggest. Finally, it is interesting to note that the integrated ADF-STEM intensity from the upper $Si_{1-y}C_y$ layers is somewhat lower than that observed in SIMS. This may be correlated with the fact that some C atoms are known to occupy nonsubstitutional sites in epitaxial $Si_{1-y}C_y$ layers with C composition in excess of 0.01. This may indicate that here the nonsubstitutional C fraction does not contribute significantly to the ADF-STEM contrast.

VI. CONCLUSION

In this study we have shown that experimental factors such as TEM sample thickness, ADF detector inner angle, and strain at the atomic scale can influence the ADF-STEM image contrast between heteroepitaxial layers and substrates. For strained $Si_{1-x}Ge_x$ layers on Si the ADF-STEM image contrast decreases with increasing thickness, and remains almost constant after the sample thickness exceeds 120 nm. The contrast was also found to increase with the increase in the ADF detector semiangle. In the $Si_{1-y}C_y/Si$ system, contrast shows an opposite thickness and ADF detector semiangle dependence of the ADF-STEM image contrast: the contrast increases with increasing sample thickness and decreases with increasing ADF detector semiangle, but the contrast remains almost constant after the sample thickness exceeds 200 nm. The dilute $Si_{1-y}C_y/Si$ system also showed some unique contrast characteristics: contradictory to the compositional contrast prediction of ADF-STEM image intensity, the lower average atomic number strained $Si_{1-y}C_y$ layers were always brighter than the higher average atomic number Si when the sample thickness is greater than 200 nm. In thinner samples, this anomalous contrast was observed for an ADF detector semiangle of up to 50 mrad. Atomic scattering calculations correctly predict the ADF-STEM image contrast dependence on the ADF detector semiangles for both $Si_{1-x}Ge_x/Si$ and $Si_{1-y}C_y/Si$ systems. Multislice simulations show that the anomalous ADF-STEM image contrast in $Si_{1-y}C_y/Si$ system can be explained by local strain effects in proximity of small radius substitutional atoms. For both materials systems, the intensity line profile of the ADF-STEM images showed excellent agreement with composition profiles obtained with analytical TEM techniques: EDX and EELS, as well as SIMS. In this context, ADF-STEM can be seen as an alternative method to quickly estimate concentration and composition fluctuations in thin layered media.

ACKNOWLEDGMENTS

The authors thank G. Parent for TEM sample preparation, S. Rolfe for the SIMS measurements, I. Sproule for the Auger measurements, and M. Robertson for providing the original multislice calculation codes.

[1] E. P. O'Reilly, Semicond. Sci. Technol. **4**, 121 (1989).
[2] P. M. Mooney and J. O. Chu, Annu. Rev. Mater. Sci. **30**, 335 (2000).
[3] D. B. Williams and C. B. Carter, *Transmission Electron Microscopy* (Plenum, New York, 1996), p. 360.
[4] D. E. Jesson, S. J. Pennycook, and J.-M. Baribeau, Phys. Rev. Lett. **66**, 750 (1991).
[5] P. Hartel, Ultramicroscopy **63**, 93 (1996).
[6] S. J. Pennycook and D. E. Jesson, Phys. Rev. Lett. **64**, 938 (1990).
[7] P. Rez and D. A. Muller, Annu. Rev. Mater. Res. **38**, 535 (2008).
[8] D. D. Perovic, C. J. Rossouw, and A. Howie, Ultramicroscopy **52**, 353 (1993).
[9] Z. Yu, D. A. Muller, and J. Silcox, J. Appl. Phys. **95**, 3362 (2004).
[10] X. Wu, M. D. Robertson, J. A. Gupta, and J.-M. Baribeau, J. Phys.: Condens. Matter **20**, 075215 (2008).
[11] J.-M. Baribeau, D. J. Lockwood, M. W. C. Dharma-Wardana, N. L. Rowell, and J. P. McCaffrey, Thin Solid Films **183**, 17 (1989).
[12] J.-M. Baribeau, D. J. Lockwood, J. Balle, S. J. Rolfe, G. I. Sproule, and S. Moisa, Thin Solid Films **410**, 61 (2002).
[13] J. C. H. Spence, *High Resolution Electron Microscopy*, 3rd ed. (Oxford University Press, New York, 2003), p. 253.
[14] M. Kawasaki, personal communication (July 2006).
[15] X. Wu, M. D. Robertson, J. A. Gupta, J.-M. Baribeau, J. C. Bennett, M. Kawasaki, and T. Aoki, Mater. Res. Soc. Symp. Proc. **982**E, KK01-03 (2007).
[16] A. C. Diebold, B. Foran, C. Kisielowski, D. A. Muller, S. J. Pennycook, E. Principe, and S. Stemmer, Microsc. Microanal. **9**, 492 (2003).
[17] D. O. Klenov and S. Stemmer, Ultramicroscopy **106**, 889 (2006).
[18] J. Liu and J. M. Cowley, Ultramicroscopy **52**, 335 (1993).
[19] J. M. Gibson, R. Hull, J. C. Bean, and M. M. J. Treacy, Appl. Phys. Lett. **46**, 649 (1985).
[20] M. M. J. Treacy and J. M. Gibson, J. Vac. Sci. Technol. B **4**, 1458 (1986).
[21] D. D. Perovic and G. C. Weatherly, Philos. Mag. A **64**, 1 (1991).
[22] J. P. Dismukes, L. Ekstrom, and R. J. Paff, J. Phys. Chem. **68**, 3021 (1964).
[23] P. C. Kelires, Phys. Rev. B **55**, 8784 (1997).
[24] L. Wang and J. M. Cowley, Ultramicroscopy **31**, 437 (1989).
[25] R. F. Egerton, *Electron Energy-Loss Spectroscopy in the Electron Microscope*, 2nd ed. (Plenum, New York, 1996), p. 134.
[26] C. R. Hall and P. B. Hirsch, Proc. R. Soc. London, Ser. A **286**, 158 (1965).
[27] C. R. Hall, P. B. Hirsch, and G. R. Booker, Philos. Mag. **14**, 979 (1966).